Supplemental Material – Bucholz et al. (2020)

Figures

Tables (see supplemental excel file)

PETROGRAPHIC DESCRIPTIONS

Ghost Lake batholith peraluminous granite

Three of the four granite samples (E19-8, SP-16-20a, SP-16-22; *Figs S1-3*) in this study are medium- to coarse-grained biotite-muscovite granites. All are two-feldspar-bearing and quartz occurs as anhedral grains with lobate boundaries or as inclusions in K-feldspar. Muscovite occurs as small laths, commonly interlocked with biotite in all samples, and occasionally or as secondary quartz+muscovite symplectites. Accessory phases include zircon, monazite, apatite, and pyrite.

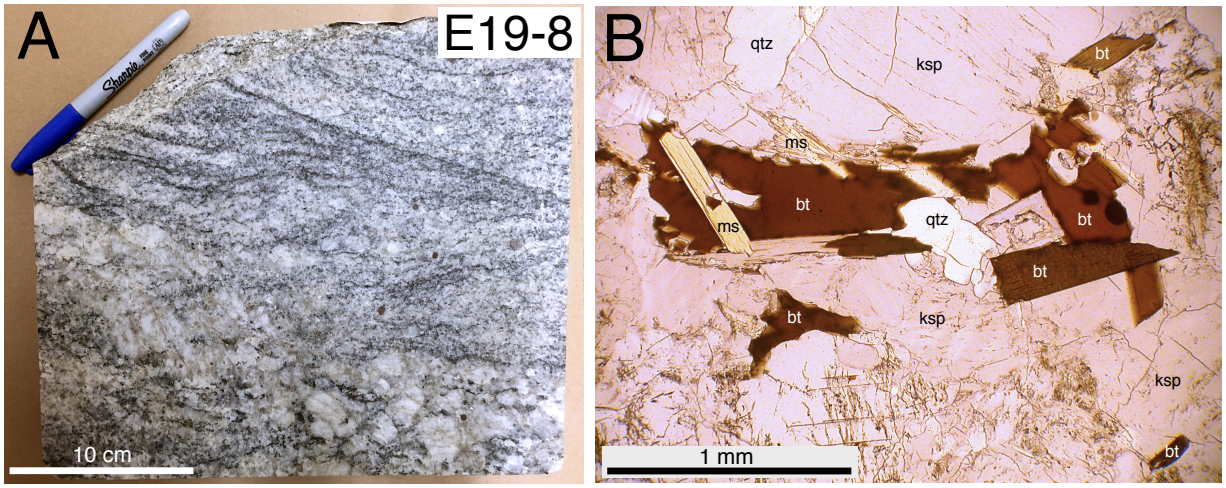

Figure S1: Sample E19-8 A) Photo of cut slab of sample. Thin section pictured in B was taken from the finer grained, foliated part of sample (upper right hand corner). Pegmatite facies of granites were avoided in this study. B) Photomicrograph showing typical interlocking textures of primary muscovite and biotite in this sample. Abbreviations: bt = biotite, ms = muscovite, ksp = K-feldspar, qtz = quartz.

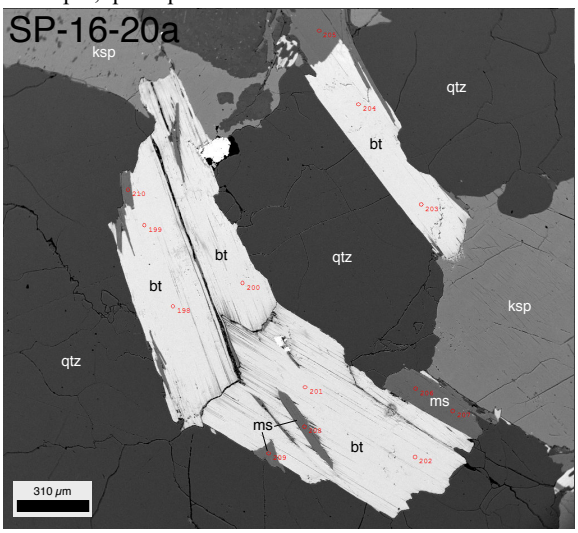

Figure S2*:* Sample SP-16-20a, Back-scatter electron (BSE) image demonstrating typical interlocking textures of biotite and muscovite. Bright inclusions in and along margins of biotite are zircons. Abbreviations as in Fig. S1

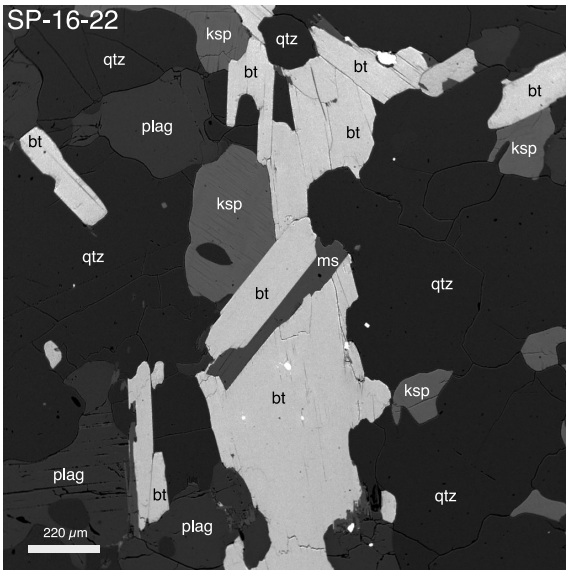

Figure S3*: Sample SP-16-22, BSE image.* Note occurrence of two feldspars. Bright inclusions in and along margins of major phases are zircon and apatite. Abbreviations: plag = plagioclase

SP-16-34 (*Fig. S4*) is a muscovite-garnet-tourmaline-biotite leucogranite dike in the host metasedimentary rocks of the Ghost Lake batholith. Primary muscovite occurs as tabular crystals with irregular terminations. Secondary muscovite is present as ragged growths on grain boundaries and in quartz-muscovite symplectite intergrowths. Biotite is a minor phase but does occur as small (<1 mm)

stubby laths. Plagioclase, K-feldspar, and quartz are all subhedral and rounded. Garnet is found in low abundances as small (100's μm in diameter) round, inclusion-free crystals. Zircon, apatite, and pyrite occur as accessory phases.

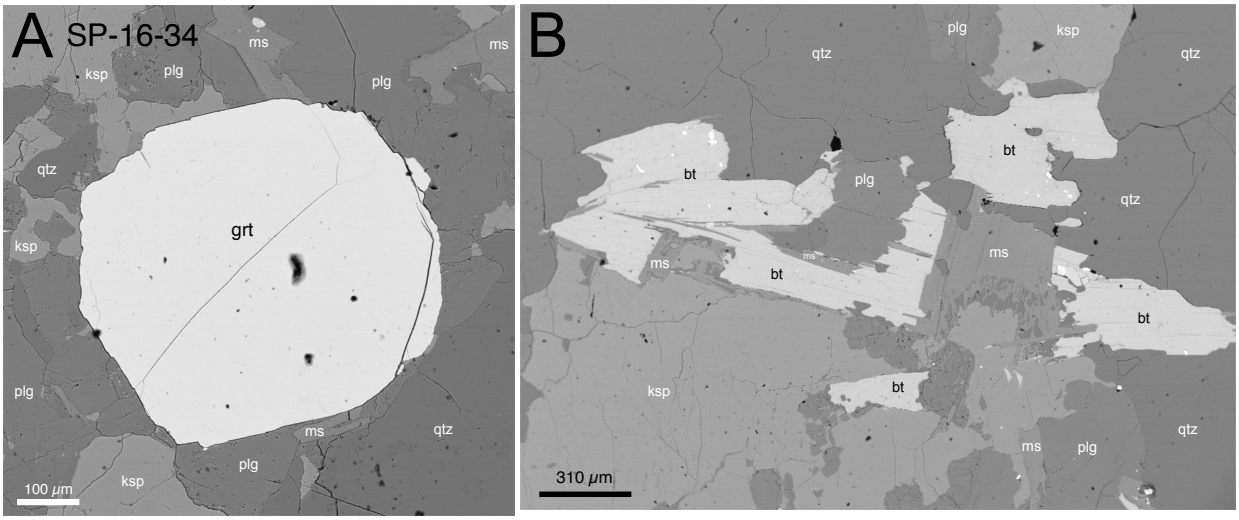

Figure S4*: Sample SP-16-34,* BSE image. A) 500-600 µm diameter, inclusion-free garnet. B) Typical textures of biotite and muscovite. Note quartz-muscovite symplectic intergrowths on termination of muscovite crystals. Bright inclusions within biotite are predominantly zircon. Abbreviations as in previous figures.

Metasedimentary units

Both metapelites and metwackes are present in all mapped isograd zones. Apatite, Fe-Ti oxides, and sulfides (pyrite and pyrrhotite) are present in all isograds as accessory phases.

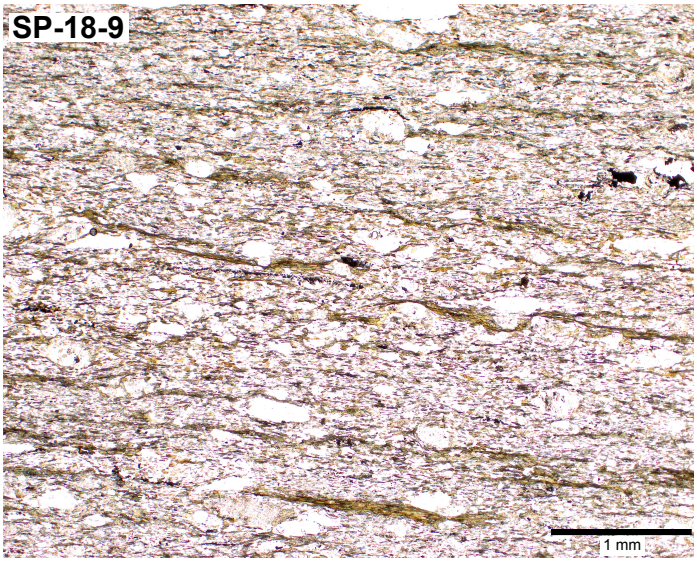

Figure S5*:* Sample SP-18-9, Transmitted light photomicrograph. Note fine-grain matrix of bioite+plagioclase+quartz with larger quartz and plagioclase clasts, as well as, elongate clusters of biotite.

Low Grade (Chlorite-Biotite Grade)

This grade is characterized by fine-grained (2-50 μm) metapelites with an assemblage of chlorite-biotite±muscovite and more common fine-to-medium-grained (2-500 μm) metawackes containing detrital plagioclase and quartz with grain diameters up to 2 mm (Breaks, 1989; Fig. S5). The wide range of grain size reflects the original range of sediment size. Minor prehnite and calcite is also present in some samples. All samples from this grade preserve original sedimentary bedding. Metamorphic foliation or other structures are not present in most samples. Occasional quartz veins are found in most samples.

Medium Grade (Andalusite and Garnet Grade)

Rocks of this grade are biotite+muscovite+plagioclase+quartz metapelites with andalusite porphyroblasts (<1 cm in diameter) (*Fig. S6*). Cordierite is also present in some samples as poikioblasts up to 2 cm long. Metawackes are more recrystallized than their chlorite-biotite zone analogs and are characterized by the appearance of garnet and disappearance of chlorite. All samples

are mildly foliated. Andalusite, cordierite, and garnet grains contain abundant quartz inclusions. These phases are typically an- to subhedral. Within this metamorphic isograd, higher grade samples show incipient replacement of andalusite with sillimanite (Fig. S6).

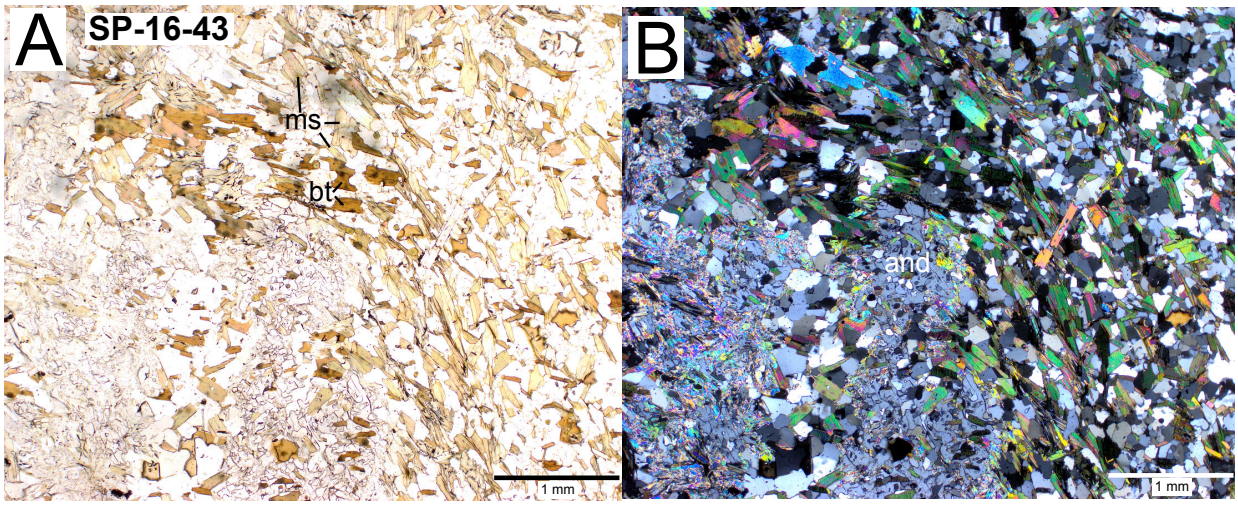

Figure S6*: Sample SP-16-43,* Photomicrographs with transmitted A) polarized light and B) cross-polarized light. Note andalusite (and) porphyroblasts with inclusions. In A, representative muscovite (ms) and biotite (bt) grains are highlighted. (Note SP-16-43 is mapped in the sillimanite-K-feldspar grade as in other parts of the samples shows incipient replacement of andalusite with sillimanite.)

High Grade (Sillimanite-K-Feldspar Grade)

Samples from this grade display evidence for partial melting, consisting of medium-grained paleosomes and coarse-medium-grained leucosomes and quartz veins (0.2-4 cm wide). Paleosomes of this grade are highly foliated and characterized by the coexistence of porphyroblastic sillimanite and K-feldspar (*Fig. S7*). Sillimanite occurs in several cm-scale aggregates in association with cordierite, biotite, K-feldspar, quartz, plagioclase, and occasionally garnet. Leucosomes are less mineralogically diverse, mainly consisting of biotite, feldspar, and quartz with occasional garnet. Metawackes on this grade are fine grained and weakly foliated. Leucosomes and quartz veins, when present, are parallel to foliation.

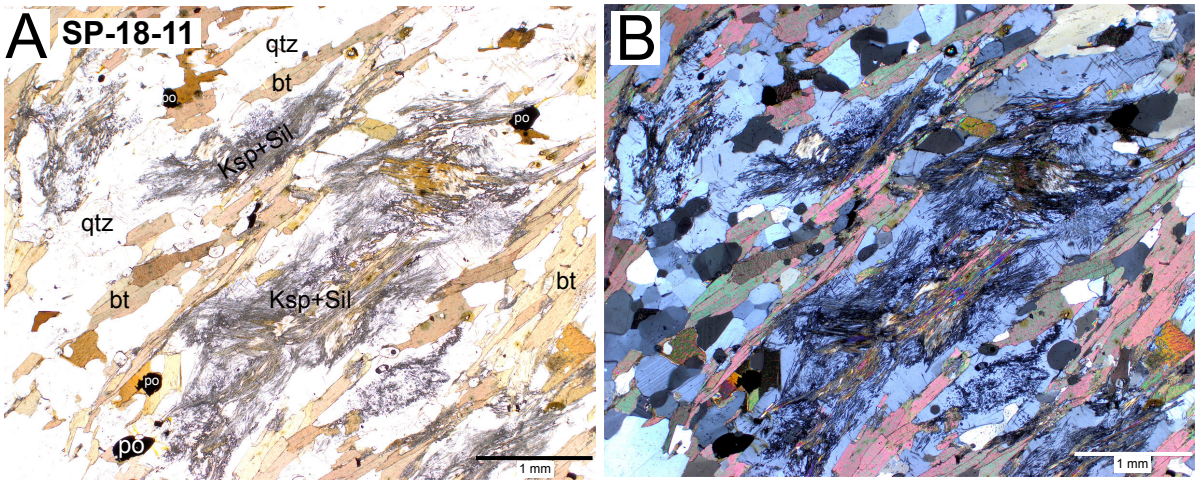

Figure S7*: Sample SP-18-11,* Photomicrographs with transmitted A) polarized light and B) cross-polarized light. Note porphyroblastic intergrowths of K-feldspar (Ksp) and sillimanite (Sil). In A, representative muscovite (ms), biotite (bt), quartz (qtz), and pyrrhotite (po) grains are highlighted.

ANALYTICAL METHODS`

X-ray fluorescence spectrometry – bulk-rock major and trace elements

Bulk-rock major and trace element concentrations were determined by X-ray fluorescence (XRF) on fused glass beads using either a ThermoARL Advant'XP+ automated sequential wavelength spectrometer at the GeoAnalytical Laboratory at Washington State University (7 samples) or using an automated Panalytical Zetium 4 kW wavelength spectrometer at Caltech (12 samples). Details of the sample preparation, analytical methods, and precision and accuracy are given in (Johnson et al., 1999) and (Bucholz and Spencer, 2019).

Electron microprobe analysis

Sulfide and silicate mineral major and minor elements were analyzed on the JEOL JXA-8200 electron microprobe at Caltech. Data were reduced using a modified ZAF pro- cedure (CITIZAF, Armstrong, 1995).

Sulfides

Fe, S, Co, Ni, Cu, and Zn concentrations in sulfides were analyzed. A 20 kV accelerating voltage, 40 nA beam current, and 10 μm beam diameter were used. Count times were 20 s on peak and 10 s on background. Primary calibration standards for the elements were: Fe and S on a natural MAC pyrite (FeS_2); Co, Cu, and Ni on pure metals; and Zn on a synthetic ZnO. Typical detection limits (wt.%) and 1σ uncertainties (percent of absolute values) were the following for each element: Fe (0.03, 0.27-0.30%), S (0.01, 0.14-0.18%), Co (0.02, 8-12%), Cu (0.03, 0.22%), and Zn (0.03, 7-9%). During analyses of unknown sulfides, Anderson pyrrhotite (Crowe and Vaughn, 1996), as well as, the EMPA pyrite standard (MAC) were measured every ~20 unknowns to monitor and correct for drift of iron-to-sulfur ratios.

Silicates

In garnet-bearing metasedimentary samples we analyzed biotite and garnet to implement garnet-biotite thermometry. For each sample, we analyzed multiple grains of each mineral (generally >10) and multiple points on each grain to explore both intra-sample and intra-grain heterogeneity. An acceleration voltage of 15 kV, a beam current of 25 nA, and a defocused beam (10 μm diameter) were used. Counting times were 40s for Mn, Ti, Cr, F, P, and Cl, and 20s for Si, Al, Mg, Fe, Ca, Na, and K. Background counting times were half of the peak counting times. The following standards were used to calibrate elemental peaks prior to each analytical session: synthetic anorthite (SiO_2, Al_2O_3, CaO), synthetic TiO_2 (TiO_2), synthetic Cr_2O_3 (Cr_2O_3), synthetic fayalite (FeO), synthetic tephroite (MnO), synthetic F-phlogopite (MgO, F), Amelia albite (Na_2O), Asbestos microcline (K_2O), Durango apatite (P), and synthetic sodalite (Cl). The detection limits for these conditions and setup were <0.01wt % for SiO_2, Al_2O_3, MgO, CaO, K_2O, P,and Cl; 0.01 wt % for TiO_2, FeO, Na_2O, and MnO; and 0.02wt % for Cr_2O_3 and F. Typical 1σ uncertainties (per cent of absolute value) on analyses calculated from counting statistics were as follows: Si, 0.25%; Ti, 2.5%; Al, 0.35 %; Fe, 0.3%; Mg, 0.55%; K, 0.35%; F, 4%. Biotite, and garnet major element compositions are given in Supplementary Data Tables S2.

Mineral separation and mounting

Samples were crushed to <250 μm. Pyrite from granitic and metasedimentary samples were obtained via heavy liquids processing of non-magnetic mineral fractions. Pyrrhotite from metasedimentary rocks were separated by hand magnet. All sulfides were then hand-picked

using a binocular microscope, mounted in epoxy, polished with lapping films and diamond suspensions to 1 μm, and carbon coated.

Secondary ion mass spectrometry (SIMS)

Please see details in main paper for SIMS analyses. Here we described the correction of instrumental mass fractionation.

Correction for Instrumental Mass Fractionation (IMF)

During analysis of pyrite, we measured three different pyrite standards; Balmat ($\delta^{34}S$ = 16.4‰; Kozdon et al., 2010), Ruttan pyrite ($\delta^{34}S$ = 1.2‰; Crowe and Vaughan, 1996), and Orocampa pyrite ($\delta^{34}S$ = 3.41‰, $\delta^{33}S$ = 1.74; these values differ from those given in Fischer et al. (2014) which was found to be in error during this study). Aliquots of the Balmat and Ruttan pyrite have been demonstrated to have $\Delta^{33}S$ of 0 (Williford et al., 2011). Note, we use the $\delta^{34}S$ value reported on bulk analysis of Balmat pyrite from (Kozdon et al., 2010) as compared to original value of 15.1‰ reported in Crowe and Vaughan, 1996 as recent studies have demonstrated the updated value to be more robust (Whitehouse, 2013). During analysis of pyrrhotite we measured Anderson pyrrhotite ($\delta^{34}S$ = 1.4±0.2‰; Crowe and Vaughan, 1996 and $\Delta^{33}S$ = 0; pers. comm. Richard Stern, U. of Alberta) and Orocampa pyrite. Raw isotope ratios were then corrected for instrumental mass fractionation (see Supplementary Material for details) using matrix-matched standards.

Standards were embedded at the center of epoxy mounts in close proximity (<3 mm) from the sample sulfides. Orocampa pyrite and Anderson pyrrhotite were used as primary standards for determining instrumental mass fractionation (IMF). A comparison of IMF for a typical analytical session of the three different pyrite standards is shown in Figure S8. IMF (α) was determined for pyrite where both $^{34}S/^{32}S$ and $^{33}S/^{32}S$ values of the standard known independently:

$$\alpha_{IMF}^{34} = (^{34}S/^{32}S)_{std-measured}/(^{34}S/^{32}S)_{std-known} \qquad \text{(Eq. 1a)}$$

$$\alpha_{IMF}^{33} = (^{33}S/^{32}S)_{st-measured}/(^{33}S/^{32}S)_{std-known} \qquad \text{(Eq. 1b)}$$

For pyrrhotite where only $^{34}S/^{32}S$ values of the Anderson pyrrhotite standard is known, $^{33}S/^{32}S$ ratios were corrected using an exponential law (Russell et al., 1978):

$$\alpha_{IMF}^{33} = [\alpha_{IMF}^{34}]^{\beta_{IMF}} \qquad \text{(Eq. 2)}$$

where the exponent β_{IMF} must be chosen to accurately represent the fractionation behavior of the instrument being used. As we only have one standard with both $^{34}S/^{32}S$ and $^{33}S/^{32}S$ measured independently by gas source IRMS limiting our ability to calculate β_{IMF} for the 7f-GEO SIMS at Caltech, we chose to follow Hauri et al. (2016) using a β_{IMF} = 0.50831 (or ln[m33/m32]/ln[m34/m32] where m_{ij} is the mass of isotope of interest, see Young et al., 2002).

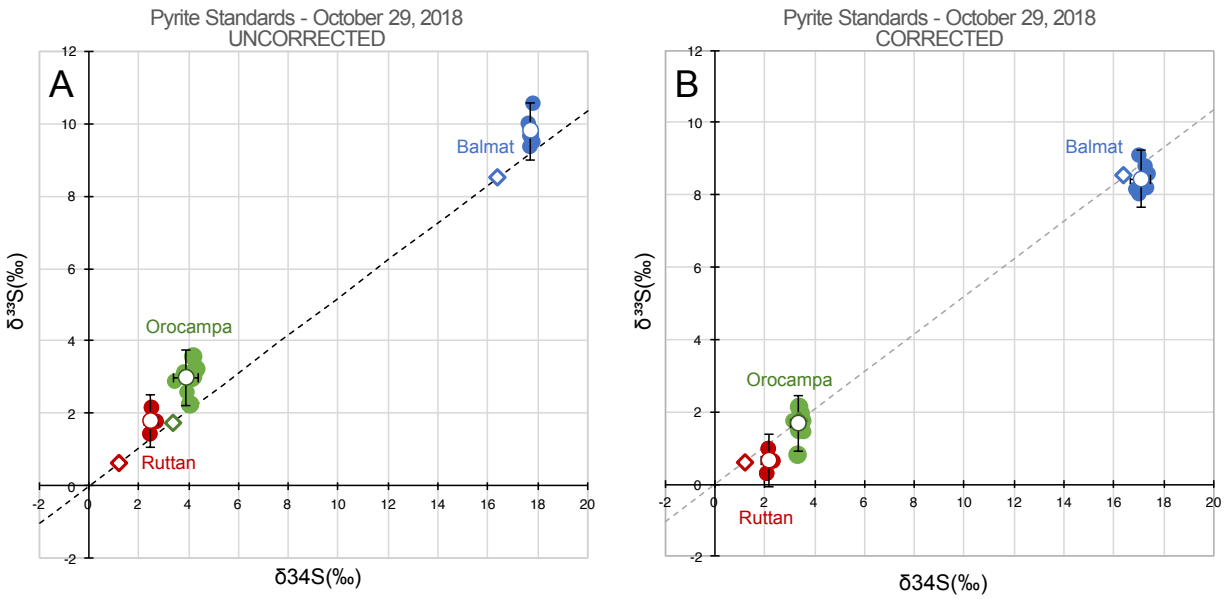

Figure S8: Comparison of instrumental mass fractionation for three pyrite standards during October 29, 2018 analytical session on the Cameca 7f-GEO at Caltech. Open diamonds indicate established value for standard. Filled circles are individual SIMS analyses. Open circles with error bars indicate average of SIMS analyses with 2σ errors. A) Raw SIMS data uncorrected for instrumental fractionation. B) Standard SIMS data corrected using IMF established for average Orocampa pyrite value.

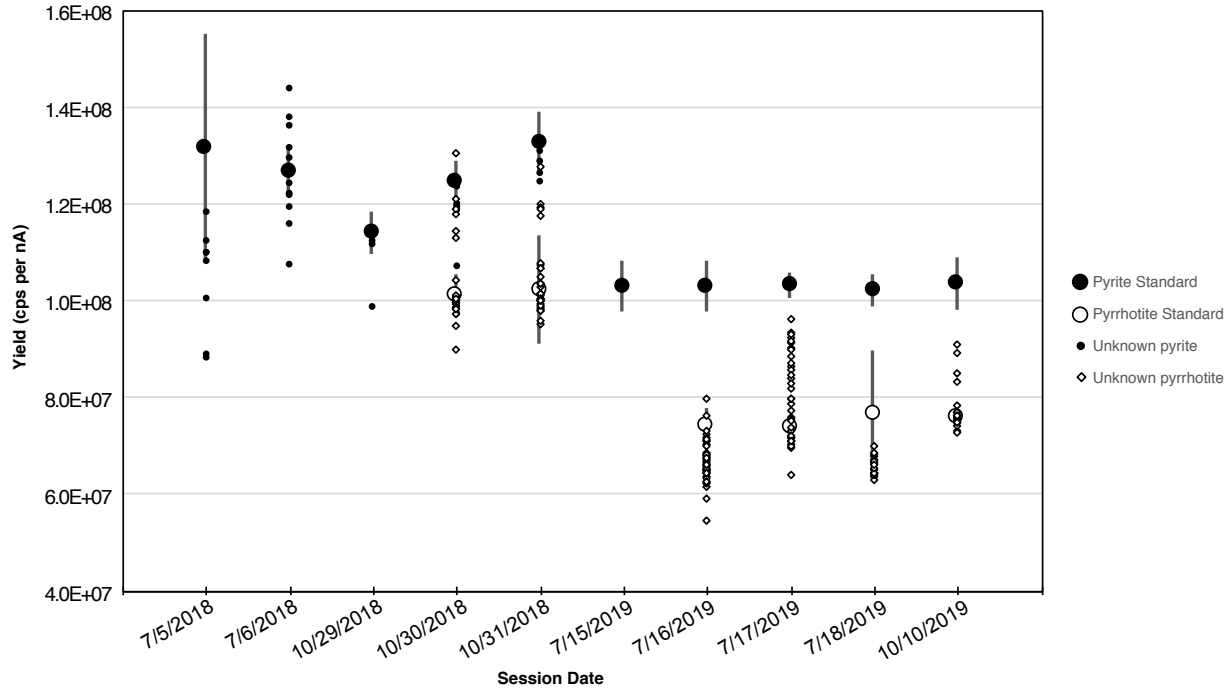

Figure S9: Comparison of yields for pyrite and pyrrhotite standards for all analytical sessions. Error bars on pyrite and pyrrhotite standards (large circles) indicate 2σ variations in yields.

Pseudosection construction

Pseudosections were constructed for most samples for which sulfur isotope data was obtained using their bulk-rock compositions and version 6.8.6 of Perple_X software (Connolly, 2009). The Perple_X software calculates equilibrium assemblage phase diagrams for fixed bulk compositions using Gibbs free energy minimization. The thermodynamic components of the modeled systems were Na_2O, MgO, Al_2O_3, SiO_2, K_2O, CaO, TiO_2, MnO, FeO, and H_2O. Fe was assumed to be completely as Fe^{2+}. The thermodynamic data set from Holland and Powell (1998, 2011) was used. All samples were assumed to be H_2O saturated. Solution models employed in the calculation of both pseudosections include: Bi(HGP) (Powell & Holland 1999), IlHm(A) (Andersen & Lindsley 1988), Gt (B) (Bergman 1990), Chl (HP) (Holland et al. 1998), and feldspar (Fuhrman and Lindsley, 1988).

Example pseudosections for representative samples are given in Supplementary Figures S10-12.

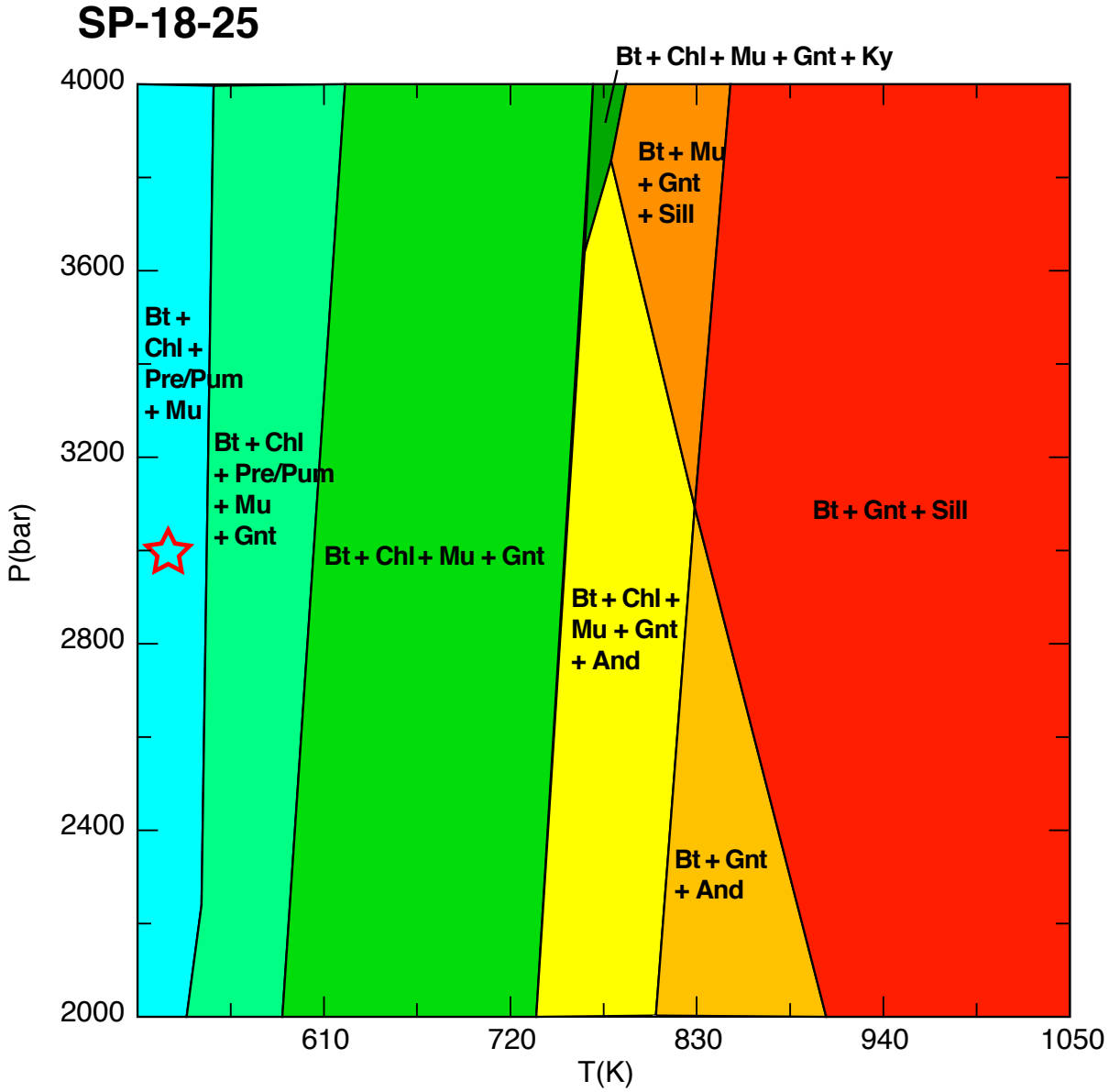

Figure S10: Pseudosection for sample SP-18-25 (biotite-chlorite grade). In addition to listed phases, quartz and feldspars are present in all fields. Rutile, Fe-Ti oxides, and titanite are present as accessory phases. At 0.3 GPa (3000 bars) the sample's phase assemblage in best reproduced at 250±20ºC (red star).

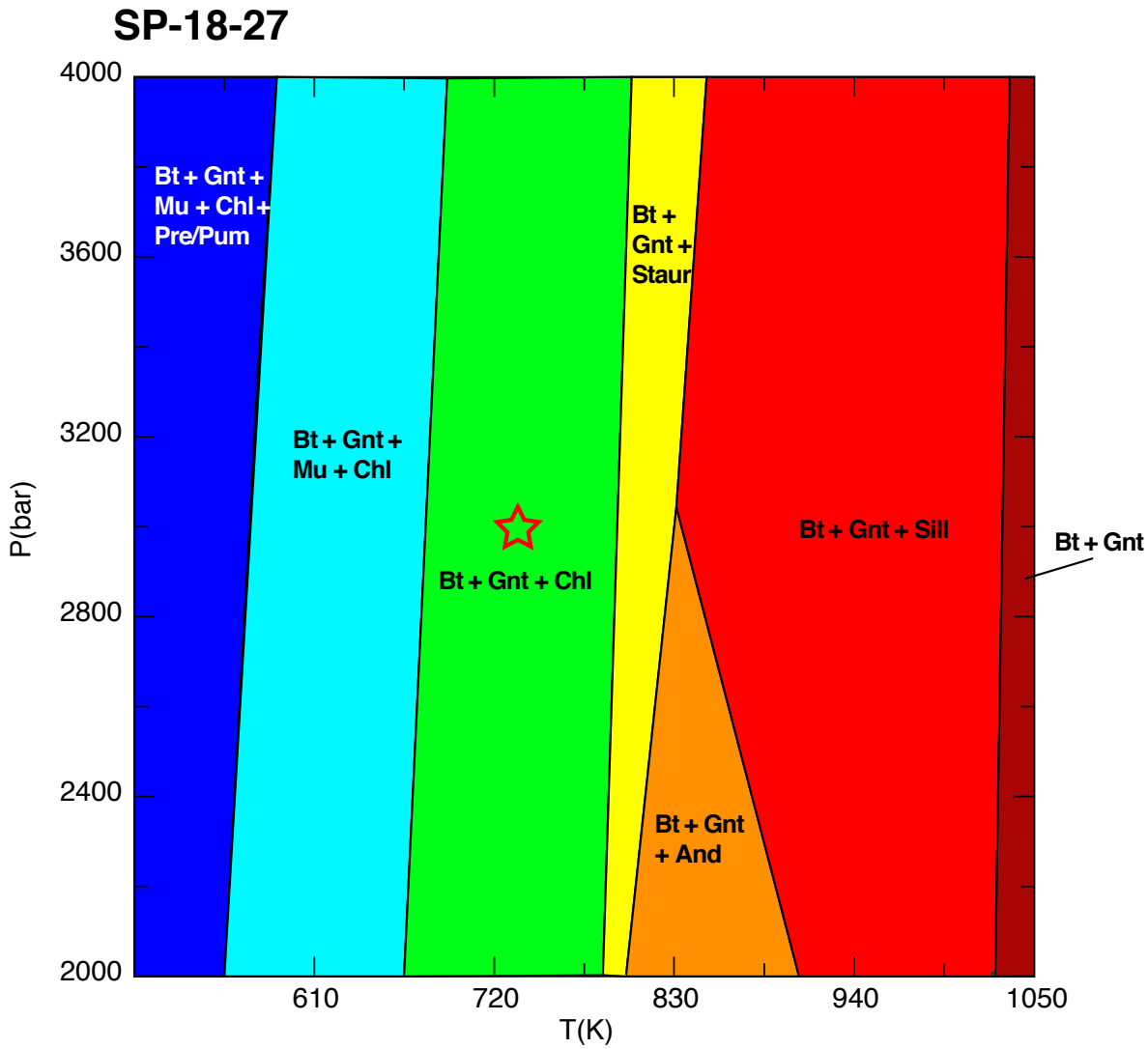

Figure S11: Pseudosection for sample SP-18-27 (garnet grade). At 0.3 GPa (3000 bars) the sample's phase assemblage is best reproduced at 510±40ºC (red star).

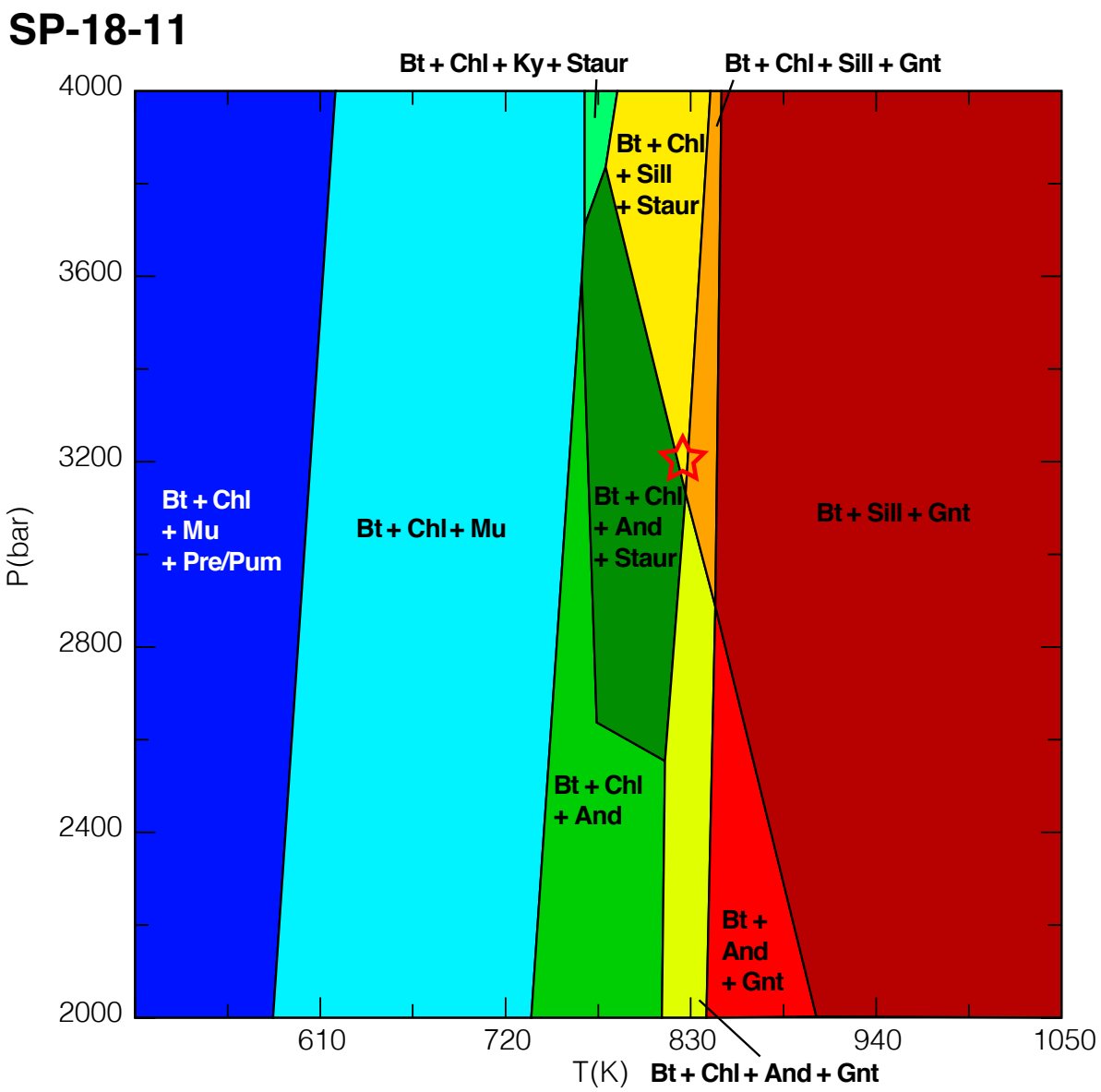

Figure S12: Pseudosection for sample SP-18-11 (K-feldspar-sillimanite grade). At 0.32 GPa (3200 bars) the sample's phase assemblage in best reproduced at 565±5ºC (red star).

REFERENCES:

Andersen, D.J. and Lindsley, D.H. (1988) Internally Consistent Solution Models for Fe-Mg-Mn-Ti Oxides - Fe-Ti Oxides. *American Mineralogist* **73**:714-26.

Armstrong, J. T. (1995). CITZAF—a package of correction pro- grams for the quantitative electron microbeam X-ray-analysis of thick polished materials, thin-films, and particles. *Microbeam Analysis* 4, 177–200.

Berman, R.G. (1990) Mixing Properties of Ca-Mg-Fe-Mn Garnets. *American Mineralogist* **75**:328-44.

Breaks, F.W., 1989. Origin and evolution of peraluminous granite and rare-element pegmatites in the Dryden Area, Superior Province of northwestern Ontario. Ph.D. thesis, Carleton Univ., Ottawa, Ontario.

Bucholz, C.E. and Spencer, C.J., 2019. Strongly Peraluminous Granites across the Archean–Proterozoic Transition. *Journal of Petrology*, *60*(7), pp.1299-1348.

Connolly, J.A.D., 1990. Multivariable phase diagrams; an algorithm based on generalized thermodynamics. American Journal of Science 290, 666–718. doi:10.2475/ajs.290.6.666

Crowe, D.E. and Vaughan, R.G., 1996. Characterization and use of isotopically homogeneous standards for in situ laser microprobe analysis of 34S/ 32S ratios. American Mineralogist 81, 187–193. doi:10.2138/am-1996-1-223

Fischer, W.W., Fike, D.A., Johnson, J.E., Raub, T.D., Guan, Y., Kirschvink, J.L. and Eiler, J.M., 2014. SQUID–SIMS is a useful approach to uncover primary signals in the Archean sulfur cycle. Proceedings of the National Academy of Sciences 111(15), 5468-5473.

Fuhrman, M. L. and Lindsley, D. H. (1988). Ternary-feldspar modeling and thermometry. *American Mineralogist*, *73*(3-4), 201-215.

Hauri, E.H., Papineau, D., Wang, J. and Hillion, F., 2016. High-precision analysis of multiple sulfur isotopes using NanoSIMS. *Chemical Geology*, *420*, pp.148-161.

Holland, T. J. B., and Powell, R. T. J. B. (1998). An internally consistent thermodynamic data set for phases of petrological interest. *Journal of Metamorphic Geology*, *16*(3), 309-343.

Holland, T. J. B., and Powell, R. (2011). An improved and extended internally consistent thermodynamic dataset for phases of petrological interest, involving a new equation of state for solids. *Journal of Metamorphic Geology*, *29*(3), 333-383.

Holland T.J.B., Baker, J., and Powell, R. (1998) Mixing properties and activity-composition relationships of chlorites in the system MgO-FeO-Al_2O_3-SiO_2-H_2O. *European Journal of Mineralogy* **10**:395-406.

Johnson, D.M., Hooper, P.R., Conrey, R.M., Laboratory, G., 1999. XRF analysis of rocks and minerals for major and trace elements on a single low dilution Li-tetraborate fused bead. Advances in X-ray Analysis 41, 843–867.

Kozdon, R., Kita, N.T., Huberty, J.M., Fournelle, J.H., Johnson, C.A., Valley, J.W., 2010. In situ sulfur isotope analysis of sulfide minerals by SIMS: Precision and accuracy, with application to thermometry of ~ 3.5 Ga Pilbara cherts. Chemical Geology 275, 243–253. doi:10.1016/j.chemgeo.2010.05.015

Powell, R. and Holland, T. (1999) Relating formulations of the thermodynamics of mineral solid solutions: Activity modeling of pyroxenes, amphiboles, and micas. *American Mineralogist* **84**:1-14.

Russell, W.A., Papanastassiou, D.A., Tombrello, T.A., 1978. Ca isotope fractionation on the Earth and other solar system materials. Geochim. Cosmochim. Acta 42, 1075–1090.

Whitehouse, M.J., 2013. Multiple Sulfur Isotope Determination by SIMS: Evaluation of Reference Sulfides for $\Delta^{33}S$ with Observations and a Case Study on the Determination of $\Delta^{36}S$. Geostandards and Geoanalytical Research 37, 19–33. doi:10.1111/j.1751-908X.2012.00188.x

Williford, K.H., Van Kranendonk, M.J., Ushikubo, T., Kozdon, R. and Valley, J.W., 2011. Constraining atmospheric oxygen and seawater sulfate concentrations during Paleoproterozoic glaciation: In situ sulfur three-isotope microanalysis of pyrite from the Turee Creek Group, Western Australia. *Geochimica et Cosmochimica Acta*, *75*(19), pp.5686-5705.

Young, E.D., Galy, A., Nagahara, H., 2002. Kinetic and equilibrium mass-dependent isotope fractionation laws in nature and their geochemical and cosmochemical significance. Geochim. Cosmochim. Acta 66 (6), 1095–1104.